



HAL
open science

Influence of the nucleation surface on the growth of epitaxial Al₂O₃ thermal CVD films deposited on cemented carbides

Maoxiang Zhu, Sofiane Achache, Mélanie Emo, Alejandro Borroto Ramírez, Jean-François Pierson, Frédéric Sanchette

► To cite this version:

Maoxiang Zhu, Sofiane Achache, Mélanie Emo, Alejandro Borroto Ramírez, Jean-François Pierson, et al.. Influence of the nucleation surface on the growth of epitaxial Al₂O₃ thermal CVD films deposited on cemented carbides. *Materials & Design*, 2022, 216, pp.110601. 10.1016/j.matdes.2022.110601 . hal-04218360

HAL Id: hal-04218360

<https://hal.science/hal-04218360>

Submitted on 26 Sep 2023

HAL is a multi-disciplinary open access archive for the deposit and dissemination of scientific research documents, whether they are published or not. The documents may come from teaching and research institutions in France or abroad, or from public or private research centers.

L'archive ouverte pluridisciplinaire **HAL**, est destinée au dépôt et à la diffusion de documents scientifiques de niveau recherche, publiés ou non, émanant des établissements d'enseignement et de recherche français ou étrangers, des laboratoires publics ou privés.



Distributed under a Creative Commons Attribution 4.0 International License



Influence of the nucleation surface on the growth of epitaxial Al_2O_3 thermal CVD films deposited on cemented carbides

Maoxiang Zhu^{a,b,c,*}, Sofiane Achache^{a,b}, Mélanie Emo^c, Alejandro Borroto Ramírez^c, Jean-François Pierson^c, Frédéric Sanchette^{a,b}

^a LASMIS, Université de Technologie de Troyes, Antenne de Nogent, Pôle Technologique de Sud Champagne, 52800 Nogent, France

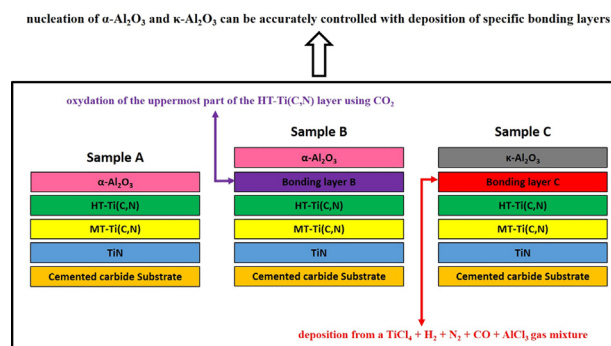
^b Nogent International Centre for CVD Innovation (NICCI), LRC CEA-LASMIS, UTT, Antenne de Nogent, Pôle Technologique de Sud Champagne, 52800 Nogent, France

^c Institut Jean Lamour, UMR CNRS 7198, Université de Lorraine, 54000 Nancy, France

HIGHLIGHTS

- The nucleation of α - and κ - Al_2O_3 can be controlled with specific nucleation treatments.
- α - Al_2O_3 is the preferred alumina phase to be deposited without any nucleation treatment.
- α - Al_2O_3 is grown epitaxially on rutile (TiO_2), with $(1\ 20)_{\alpha\text{-Al}_2\text{O}_3} // (10\ 1)_{\text{rutile}}$, $(003)_{\alpha\text{-Al}_2\text{O}_3} // (010)_{\text{rutile}}$ and $[210]_{\alpha\text{-Al}_2\text{O}_3} // [101]_{\text{rutile}}$.
- κ - Al_2O_3 is grown epitaxially on $\text{Ti}(\text{C}, \text{N})$, with $(100)_{\kappa\text{-Al}_2\text{O}_3} // (1\ 1\ 1)_{\text{Ti}(\text{C}, \text{N})}$, $(0\ 1\ 3)_{\kappa\text{-Al}_2\text{O}_3} // (2\ 20)_{\text{Ti}(\text{C}, \text{N})}$ and $[031]_{\kappa\text{-Al}_2\text{O}_3} // [112]_{\text{Ti}(\text{C}, \text{N})}$.

GRAPHICAL ABSTRACT



ARTICLE INFO

Article history:

Received 12 November 2021

Revised 17 February 2022

Accepted 25 March 2022

Available online 17 March 2021

Keywords:

Thermal chemical vapor deposition (CVD)

Alumina

Epitaxial growth

Bonding layer

ABSTRACT

This work aims at understanding the nucleation and growth of alumina films grown on $\text{Ti}(\text{C}, \text{N})$ -based layers using an industrial-scale CVD system. Firstly, Al_2O_3 layer was deposited on $\text{Ti}(\text{C}, \text{N})$ -based layers without any nucleation treatment, pure α - Al_2O_3 is obtained, whereas no orientation relationship at the $\text{Ti}(\text{C}, \text{N})/\alpha$ - Al_2O_3 layers interface can be observed. Secondly, Al_2O_3 layer was deposited on the bonding layer consisting of rutile TiO_2 , which is obtained by oxidizing the uppermost part of $\text{Ti}(\text{C}, \text{N})$ -based layers. Herein, α - Al_2O_3 single-phased layer is obtained, and the epitaxial growth of α - Al_2O_3 on rutile is observed. The orientation relationships can be found as: $(1\ 20)_{\alpha\text{-Al}_2\text{O}_3} // (10\ 1)_{\text{rutile}}$, $(003)_{\alpha\text{-Al}_2\text{O}_3} // (010)_{\text{rutile}}$ and $[210]_{\alpha\text{-Al}_2\text{O}_3} // [101]_{\text{rutile}}$. Finally, Al_2O_3 layer was deposited on the bonding layer, produced from a TiCl_4 - H_2 - N_2 - CH_4 - CO - AlCl_3 gas mixture. Regarding this intermediate layer, despite additions of CO and AlCl_3 , no evidence for oxide phases, e.g. TiO_2 and Al_2O_3 can be found, while $\text{Ti}(\text{C}, \text{N})$ needle-shaped grains develop. In this case, κ - Al_2O_3 is epitaxially grown on $\text{Ti}(\text{C}, \text{N})$, with the orientation relationships found as: $(0\ 1\ 3)_{\kappa\text{-Al}_2\text{O}_3} // (2\ 20)_{\text{Ti}(\text{C}, \text{N})}$, $(100)_{\kappa\text{-Al}_2\text{O}_3} // (1\ 1\ 1)_{\text{Ti}(\text{C}, \text{N})}$ and $[031]_{\kappa\text{-Al}_2\text{O}_3} // [112]_{\text{Ti}(\text{C}, \text{N})}$. Since processing parameters for the alumina depositions were always the same, it is revealed that the nucleation of α - Al_2O_3 and κ - Al_2O_3 can be accurately controlled with deposition of specific bonding layers.

© 2022 The Authors. Published by Elsevier Ltd. This is an open access article under the CC BY license (<http://creativecommons.org/licenses/by/4.0/>).

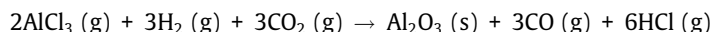
1. Introduction

Coated cutting tools are widely used in the metal cutting industry, in order to improve productivity and process reliability [1,2]. In

* Corresponding author at: LASMIS, Université de Technologie de Troyes, Antenne de Nogent, Pôle Technologique de Sud Champagne, 52800 Nogent, France.

E-mail address: maoxiang.zhu@utt.fr (M. Zhu).

this respect, CVD Al₂O₃ coatings are considered as an ideal candidate, owing to the beneficial combination of good chemical inertness and hardness at high temperature [3–7]. CVD Al₂O₃ coatings are commonly deposited from a AlCl₃-CO₂-H₂-H₂S-HCl gas mixture [8–12]. The global process can be described by the following reaction:



This overall reaction involves both homogeneous gas phase reactions and heterogeneous surface reactions [13]. Additionally, the introduction of catalyst H₂S may enhance the overall reaction rate and suppress the “dog-bone” effect to gain a better thickness uniformity [13–15].

Accordingly, κ -Al₂O₃ and α -Al₂O₃ are desired for cutting applications [5,6]. The metastable κ -Al₂O₃ has an orthorhombic structure (space group Pna2₁) with lattice parameters $a = 4.84 \text{ \AA}$, $b = 8.33 \text{ \AA}$ and $c = 8.95 \text{ \AA}$, showing an -ABAC- stacking sequence of oxygen close-packed planes along the c -axis, Al-ions occupy both tetrahedral and octahedral interstitial sites at a 1:3 ratio [16]. The stable α -Al₂O₃ has a trigonal crystal structure (space group R3c) with lattice parameters $a = b = 4.75 \text{ \AA}$ and $c = 12.97 \text{ \AA}$ [17]. The structure consists of an -ABAB- stacking sequence of oxygen close-packed planes with Al-ions in octahedral interstices. Importantly, κ -Al₂O₃ may transform irreversibly to α -Al₂O₃ resulting in volume contraction of about 8%, due to the heat generated during the CVD process as well as metal cutting [18]. Furthermore, it is found that mechanical properties of CVD α -Al₂O₃ coatings can be enhanced by choosing an optimized texture for the α -Al₂O₃ phase [12,13]. Thus, CVD Al₂O₃ coatings have continuously been optimized with respect to the phase and film texture control [12,19,20].

Because of adhesion problems between Ti(C,N)-based layers and Al₂O₃ layers, the use of bonding layers is suggested to enhance the toughness of tools and achieve the growth control of alumina [21–25]. Halvarsson *et al* show that the nucleation of κ -Al₂O₃ is favorably occurring on non-oxidized surfaces of Ti(C,N) [26,27]. Despite α -Al₂O₃ shows excellent thermal stability compared to κ -Al₂O₃, it is found to be difficult to be deposited directly on Ti(C,N)-based layers [21–24]. It is also reported that deposition of the bonding layer consisting of titanium oxides, *e.g.* Ti₂O₃ or Ti₄O₇, between Ti(C,N)-based and Al₂O₃ layers can promote the growth of α -Al₂O₃ [5,6]. However, the basic mechanisms explaining why the nucleation of α -Al₂O₃ is favored by different oxidizing treatment steps and bonding layers are not well known.

In this work, three Al₂O₃ coatings without and with bonding layers corresponding to samples: **A**, **B** and **C** were performed. Two other coatings corresponding to samples: **B1** and **C1** were stopped after synthesis of the bonding layers **B** and **C**. Firstly, X-ray diffraction was used for phase identification. The surface morphologies were observed by scanning electron microscopy (SEM), and the film cross-sectional microstructures were investigated by transmission electron microscopy (TEM). The orientation relationships at the Ti(C,N)/Al₂O₃ or bonding/Al₂O₃ layers interface were studied by high resolution transmission electron microscopy (HRTEM).

2. Materials and methods

2.1. Sample preparation

All coatings were deposited on cemented carbide substrates (WC-Co 6 wt%) mirror polished (1 μm diamond slurry), using an industrial-scale low-pressure CVD system (Ionbond Bernex™ BPXpro 325S). The global process has been described in a previous

work [28]. The device is mainly composed of five systems: reactor chamber, gaseous precursors supply system, liquid precursors (TiCl₄ and CH₃CN) supply system, AlCl₃ generator and by-products treatment system, note that the *in-situ* chlorination of Al-pellets generates almost only AlCl₃ and its dimer Al₂Cl₆ under experimental conditions used [28]. The detailed parameters are given in Table 1.

The multilayered coatings consist of a 0.5 μm -thick TiN inner layer, followed by a 2.5 μm -thick medium temperature Ti(C,N) layer, a 0.5 μm -thick high temperature Ti(C,N) layer, and a 4 μm -thick Al₂O₃ layer. The so-called medium temperature Ti(C,N) (MT-Ti(C,N)) layer was deposited at 850 °C from a TiCl₄-CH₃CN-H₂-N₂ gas mixture, whereas the high temperature Ti(C,N) (HT-Ti(C,N)) layer was deposited at 1005 °C from a TiCl₄-CH₄-H₂-N₂ gas mixture.

In sample **A**, Al₂O₃ top layer was deposited on Ti(C,N)-based layers without any nucleation treatment. On the contrary, Al₂O₃ layer in sample **B** was deposited on the bonding layer **B**, which was obtained by oxidizing the uppermost part of the HT-Ti(C,N) layer using CO₂. Al₂O₃ layer in sample **C** was deposited on the bonding layer **C**, which was produced from a TiCl₄-H₂-N₂-CH₄-CO-AlCl₃ gas mixture. Two other coatings (samples **B1** and **C1**) were stopped after synthesis of the bonding layers **B** and **C**.

2.2. Characterization

X-ray diffraction (XRD) studies were carried out using a Bruker D8 Advance diffractometer operating at 40 kV/40 mA with K α radiation of Cu (λ K α ₁ = 1.54059 \AA and λ K α ₂ = 1.54443 \AA), phase identifications were conducted in Bragg-Brentano geometry with a step size of 0.02° for a 2θ -range from 20° to 60°. The peak positions were determined by fitting the diffraction peaks with Pseudo-Voigt function after K α ₂ stripping. The software MAUD was used, the instrumental effect has been considered. For clarity, the standard material[®] 640d is used as reference to determine the instrumental contribution, as the crystallite size of the standard material is known.

The surface morphologies were observed by scanning electron microscopy (SEM) using a Zeiss Gemini 500. Transmission electron microscopy (TEM) analyses were performed in a JEOL JEM-ARM 200F Cold FEG TEM/STEM equipped with a spherical aberration (Cs) probe corrector operating at 200 kV. STEM micrographs were obtained using high angle annular dark field (HAADF) detectors. Electron energy loss spectroscopy (EELS) analyses were performed for differently grown layers. The orientation relationships at the Ti(C,N)/Al₂O₃ layers interface were investigated by high-resolution transmission electron microscopy (HRTEM). Prior to TEM investigations, all cross-sectional thin foils were prepared using a FIB/SEM FEI Helios NanoLab 600i equipped with platinum gas injection system. FIB column used a gallium liquid metal ion source operating at an accelerating voltage up to 30 kV, and a Pt-layer was deposited to protect the sample surface, using the commercial FEI MeCpPtMe3 precursor.

3. Results and discussion

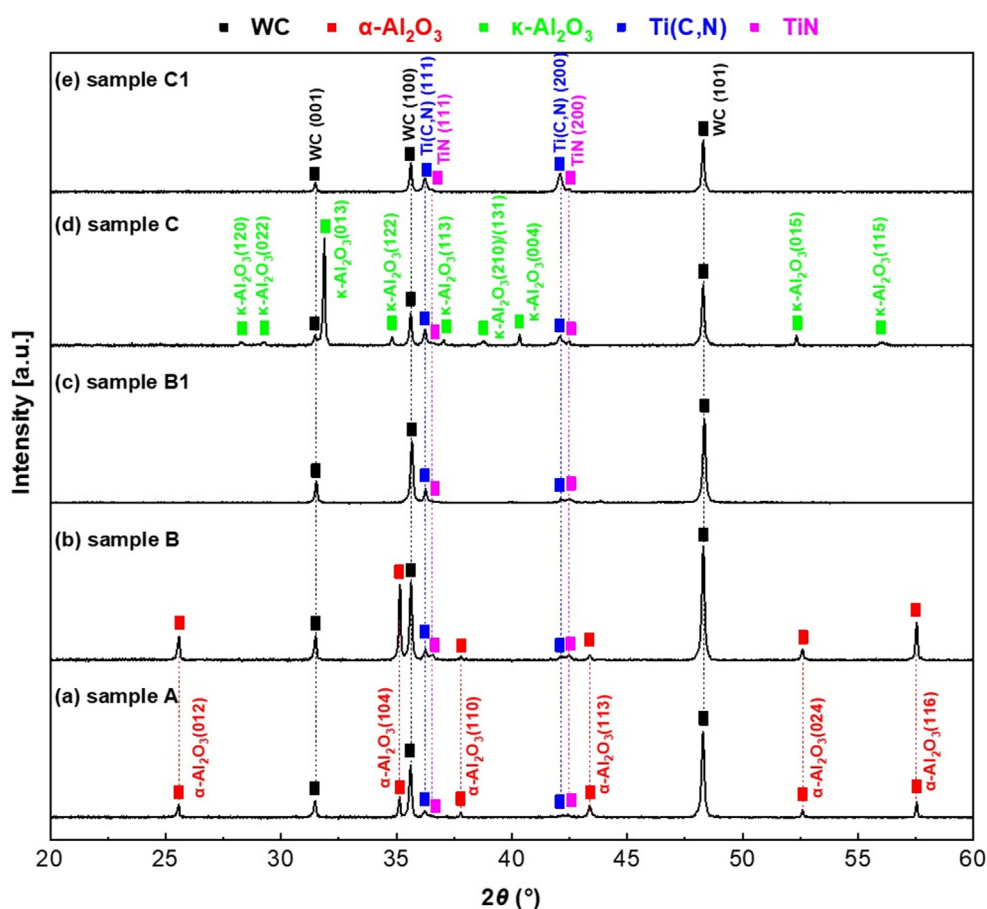
3.1. X-ray diffraction

The X-ray diffractograms of samples **A**, **B**, **B1**, **C** and **C1** are shown in Fig. 1 (a) – (e). As for sample **B1**, it was stopped after synthesis of the bonding layer **B**. Since the bonding layer is thin (approx. 100 nm), peaks corresponding to titanium oxides in the 2θ region investigated exhibit insufficient intensity. To highlight the growth of rutile, sample **B1** was investigated by TEM, the SAED pattern is presented in Supplementary Fig. S1.

Table 1

The detailed processing parameters are given, a series of coatings were performed: sample **A**: TiN/MT-Ti(C,N)/HT-Ti(C,N)/Al₂O₃ sample **B**: TiN/MT-Ti(C,N)/HT-Ti(C,N)/bonding layer **B**/Al₂O₃ sample **B1**: TiN/MT-Ti(C,N)/HT-Ti(C,N)/bonding layer **B** sample **C**: TiN/MT-Ti(C,N)/HT-Ti(C,N)/bonding layer **C**/Al₂O₃ sample **C1**: TiN/MT-Ti(C,N)/HT-Ti(C,N)/bonding layer **C**.

	TiN	MT-Ti(C,N)	HT-Ti(C,N)	bonding layer B	bonding layer C	Al ₂ O ₃
Temperature (°C)	900	850	1005	1005	1005	1005
Pressure (mbar)	70	70	70	70	70	70
Time (min)	40	60	20	20	20	150
H ₂ (vol.%)	balance					
N ₂ (vol.%)	39.6	20.3	18.4	-	9.2	-
TiCl ₄ (vol.%)	1.3	2.4	1.4	-	1.2	-
CH ₃ CN (vol.%)	-	0.8	-	-	-	-
CH ₄ (vol.%)	-	-	3.4	-	2.2	-
CO ₂ (vol.%)	-	-	-	3.8	-	4.0
CO (vol.%)	-	-	-	-	0.9	-
AlCl ₃ (vol.%)	-	-	-	-	0.4	1.6
HCl (vol.%)	-	-	-	-	-	2.0
H ₂ S (vol.%)	-	-	-	-	-	0.3
Total gas flow (L.min ⁻¹)	33.8	26.1	32.5	26.0	32.5	25.0

**Fig. 1.** X-ray diffractograms of samples **A**, **B**, **B1**, **C** and **C1**.

As shown in Fig. 1, the WC phase and the Ti(C,N) phase are indexed by the ICDD powder diffraction files 01-073-9900 and 01-071-6059, respectively. Ti(C,N) (111) and (200) peaks neighbour closely two other reflections belonging to the TiN layer underneath, minor overlaps near the baseline among these reflections are observed. Additionally, since the main advantage of the MT-CVD Ti(C,N) process is the suppression of interfacial η -phase, e.g. W₃Co₃C or W₆Co₆C, which is not detected, consistent with earlier studies [29–31].

Without any nucleation treatment, pure α -Al₂O₃ is obtained in sample **A** (see Fig. 1 (a)). It is shown that the deposition of bonding layer **B** also leads to the growth of α -Al₂O₃ (see Fig. 1 (b)). Further-

more, it is revealed that the deposition of bonding layer **C** promotes the nucleation of κ -Al₂O₃ in sample **C** (see Fig. 1 (d)). Sample **C1** was stopped after synthesis of the bonding layer **C**, no evidence for oxide phases can be found herein. The α -Al₂O₃ and κ -Al₂O₃ phases are indexed by the ICDD powder diffraction files 00-046-1212 and 00-052-0803, respectively.

3.2. Surface morphology

Fig. 2 (a) – (c) show the surface morphologies of samples **A**, **B** and **C**, samples **A** and **B** exhibit similar morphologies composed of small faceted grains. Previous studies found that the κ - to α -

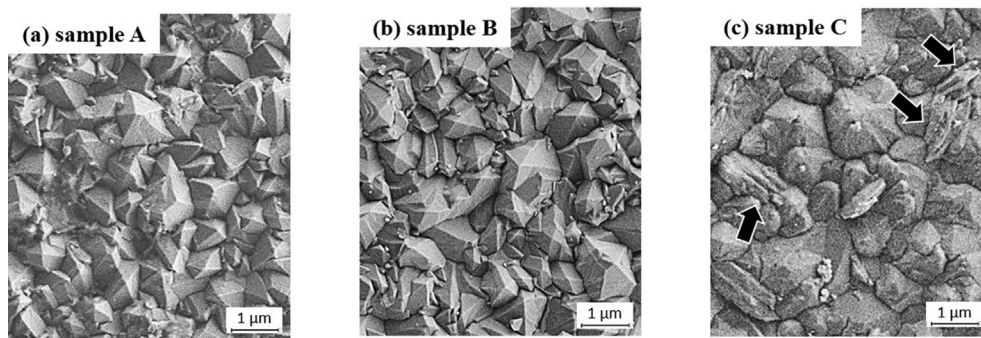


Fig. 2. SEM micrographs (a) – (c) showing surface morphologies of samples A, B and C. Some twin-related defects (black arrows) of κ - Al_2O_3 are observed in the SEM micrograph (c).

Al_2O_3 phase transformation often occurs, this process depends strongly on the deposition time and temperature [2,22,32]. It is also observed that the α - Al_2O_3 obtained through the phase transformation exhibits relatively large equiaxed grains [2]. In addition, thermal stability of κ - Al_2O_3 coatings was studied previously by heat treatment at 1000 °C, while argon (Ar) was used as a carrier gas, it is found that the phase transformation started at 70 min [33]. However, neither diffraction peak originating from κ - Al_2O_3 (see Fig. 1 (a) and (b)), nor large equiaxed grains can be observed (see Fig. 2 (a) and (b)). Hence, no phase transformation can be expected in samples A and B. Meanwhile, twin-related defects typically present in κ - Al_2O_3 are visible in the SEM micrograph of sample C (see Fig. 2 (c)), in agreement with an earlier study [19].

3.3. Microstructural analyses

Fig. 3 (a) is a cross-section STEM HAADF micrograph of sample A, and Fig. 3 (b) shows EELS mapping acquired from the dashed square indicated in (a). Since acetonitrile (CH_3CN) is considered as the single carbon and nitrogen feeding source, it is generally accepted that the C/(C + N) ratio of MT-Ti(C,N) coatings is almost independent from deposition parameters and it is typically around 0.5 [34,35]. However, the chemical composition of HT-Ti(C,N) coatings is highly reliant on CH_4 and N_2 contents in the gas mixture [36]. Herein, a relatively low CH_4/N_2 ratio was used for the deposi-

tion of the HT-Ti(C,N) layer. Therefore, the MT-Ti(C,N) layer is carbon-rich and the HT-Ti(C,N) layer is nitrogen-rich, as shown in Fig. 3.

Fig. 4 (a) shows a cross-section TEM BF image of sample A, and Fig. 4 (b) is a TEM BF image with lower magnification to present the entire Al_2O_3 layer, which is approximately 4 μm -thick. Fig. 4 (b.1) is a SAED pattern acquired from the pink circle area indicated in Fig. 4 (b). This diffraction pattern evidences the formation of α - Al_2O_3 . Fig. 4 (c) shows a TEM BF image acquired from the red circle area indicated in Fig. 4 (a), at the HT-Ti(C,N)/ α - Al_2O_3 layers interface. Fig. 4 (c.1) and (c.2) present SAED patterns acquired from the pink and green circle areas indicated in Fig. 4 (c), α - Al_2O_3 is grown on the HT-Ti(C,N) layer. Furthermore, detailed analysis was carried out using high resolution transmission electron microscopy (HRTEM), but no orientation relationship at the HT-Ti(C,N)/ α - Al_2O_3 layers interface can be highlighted.

As mentioned beforehand, the metastable κ - Al_2O_3 phase should be the preferred alumina phase grown on non-oxidized surfaces of Ti(C,N), with the epitaxial growth of {001} κ - Al_2O_3 close-packed planes on {111} Ti(C,N) [19,21]. Apparently, it is not always the case. It is also reported that the κ - to α - Al_2O_3 phase transformation initiated at free surfaces, e.g. interfacial voids, often occurs in a CVD reactor resulting in pronounced cracking [2]. However, no visible cracking along the grain boundaries can be observed. Thereby, the phase transformation is ruled out, and it can be speculated that

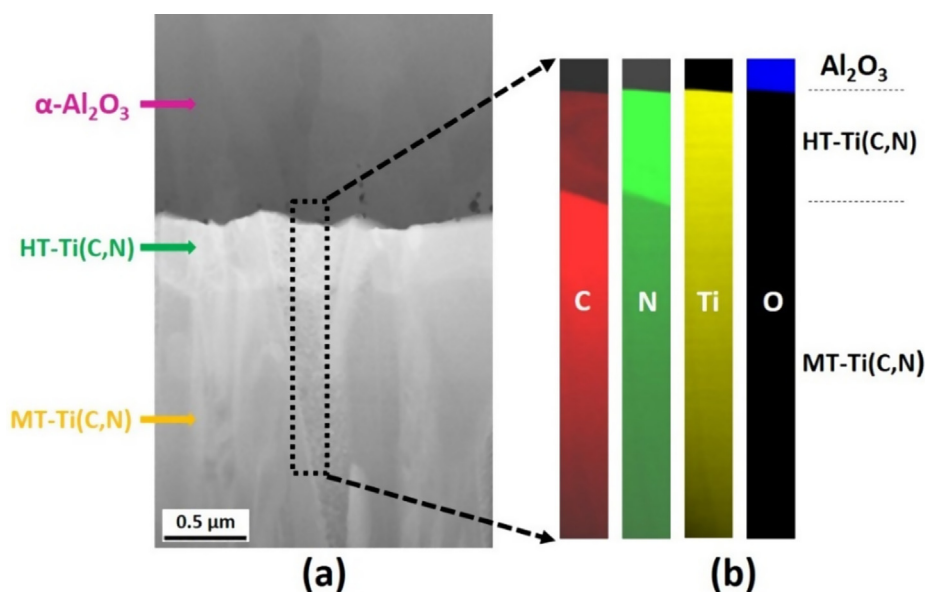


Fig. 3. (a) STEM HAADF micrograph showing a cross-section of sample A. (b) EELS mapping obtained from the black dashed square indicated in (a).

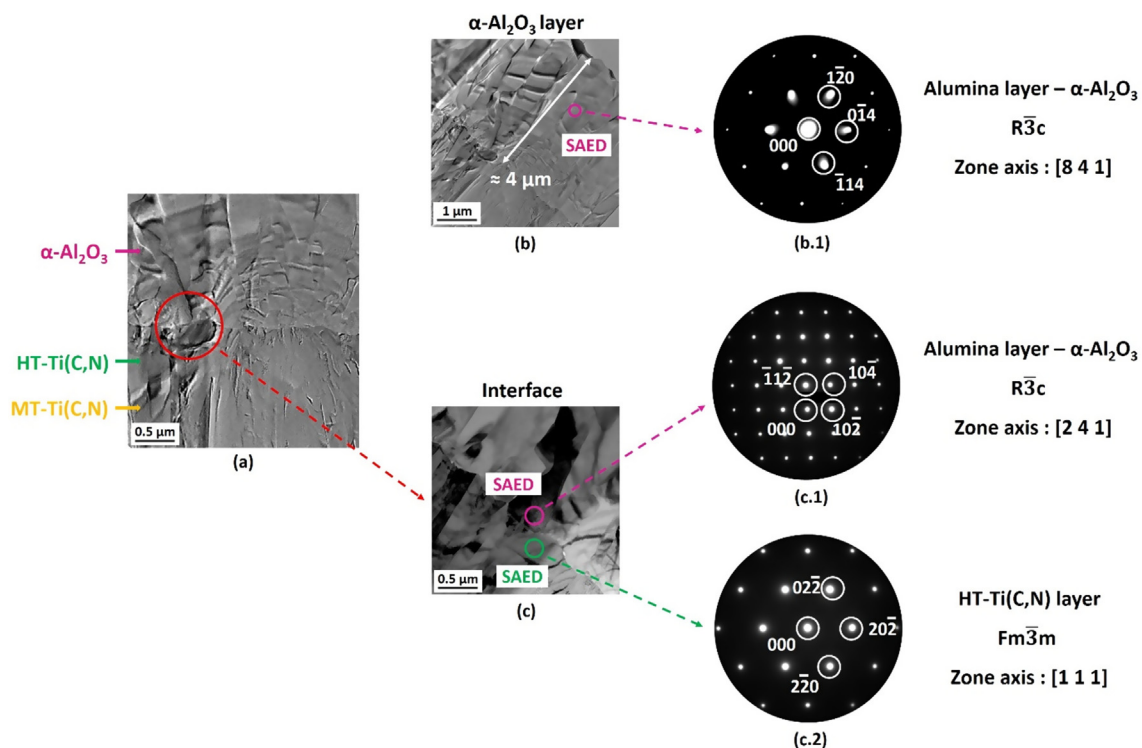


Fig. 4. (a) TEM BF image showing a cross-section overview of sample **A**. (b) TEM BF image with lower magnification to present the entire Al_2O_3 layer. (c) TEM BF image acquired from the red circle area at the interface indicated in (a). (b.1), (c.1) and (c.2) are selected area electron diffraction (SAED) patterns corresponding to differently grown layers. (For interpretation of the references to colour in this figure legend, the reader is referred to the web version of this article.)

since $\alpha\text{-Al}_2\text{O}_3$ is the most thermodynamically stable phase, it is favorably occurring with the deposition conditions used in the current study.

Fig. 5 (a) is a cross-section STEM HAADF micrograph of sample **B**, and Fig. 5 (b) shows EELS mapping acquired from the black dashed square indicated in Fig. 5 (a). From EELS analyses, the bonding layer **B** consisting of TiO_2 is highlighted between the HT-Ti(C,N) and Al_2O_3 layers. As the deposition parameters were always the same for Ti(C,N)-based layers, the carbon-rich MT-Ti(C,N) and nitrogen-rich HT-Ti(C,N) layers are evidenced.

Fig. 6 (a) shows a cross-section TEM BF image of sample **B**, almost the entire Al_2O_3 layer is composed of large columnar grains. It is reported that the grain refinement at the start of $\alpha\text{-Al}_2\text{O}_3$ growth can be achieved by the oxidizing treatment using a gas mixture of CO_2 and CO [15]. Herein, the uppermost part of the HT-Ti(C,N) layer was oxidized without CO, few small grains can thus be observed, whereas some interfacial voids are found at the bonding/ $\alpha\text{-Al}_2\text{O}_3$ layers interface indicated by black arrows in Fig. 6 (a). It is assumed that the volume contraction of the order of 25–30% associated with the phase transformation of titanium

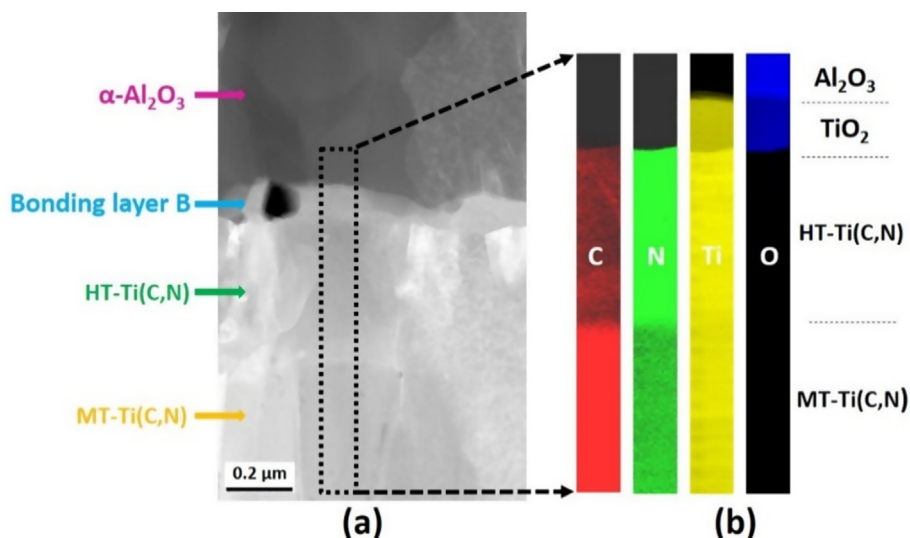


Fig. 5. (a) STEM HAADF image showing a cross-section of sample **B**. (b) EELS mapping acquired from the black dashed square indicated in (a).

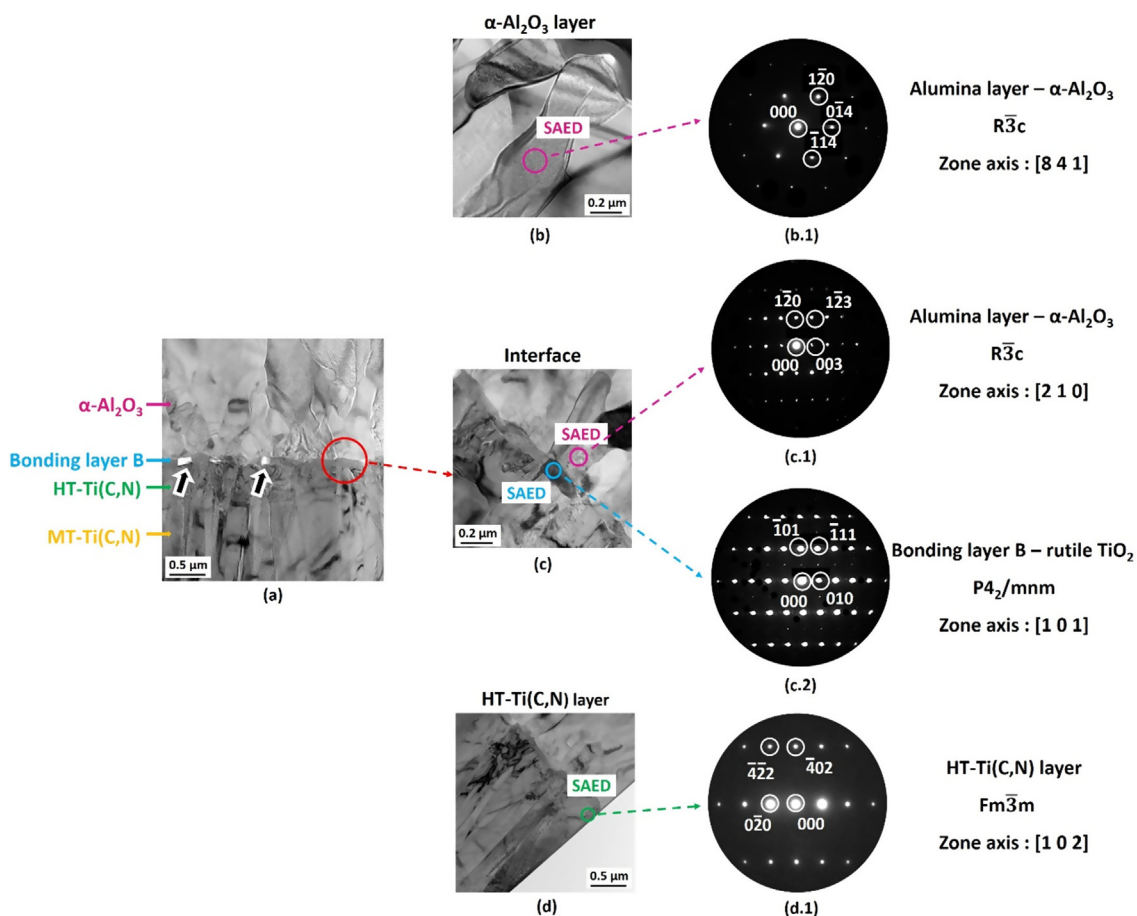


Fig. 6. (a) TEM BF image showing a cross-section overview of sample **B**. Some porosity at the interface are observed (indicated by arrows). (b) and (d) TEM BF images showing the α -Al₂O₃ and HT-Ti(C,N) layers. (c) TEM BF image acquired from the red area at the bonding/ α -Al₂O₃ layers interface indicated in (a). (b.1)-(d.1) SAED patterns corresponding to different layers. (For interpretation of the references to colour in this figure legend, the reader is referred to the web version of this article.)

oxides, due to the interdiffusion of the bonding and Ti(C,N)-based layers [6,15].

Fig. 6 (b) presents a TEM BF image of Al₂O₃ layer near the coating surface, and Fig. 6 (b.1) is a SAED pattern acquired from the pink circle area indicated in Fig. 6 (b). Fig. 6 (c) shows a TEM image at the bonding/ α -Al₂O₃ layers interface acquired from the red circle area indicated in Fig. 6 (a). As shown in Fig. 6 (c.1) and (c.2), SAED patterns reveal the growth of α -Al₂O₃ on the rutile bonding layer. Titanium dioxide (TiO₂) crystallizes primarily in three different phases, rutile, anatase and brookite, among which rutile state (tetragonal, space group P4₂/mnm, with lattice parameters $a = b = 4.59$ Å and $c = 2.96$ Å) is the most stable one [37]. Herein, sample **B1** was stopped after synthesis of the bonding layer **B**, and the growth of rutile is evidenced (see Supplementary Fig. S1).

Fig. 7 (a) shows a TEM image at the bonding/ α -Al₂O₃ layers interface, the rutile bonding layer is approximately 107 nm-thick. Fig. 7 (b) is a HRTEM image obtained from the yellow square indicated in Fig. 7 (a), where the epitaxial growth of α -Al₂O₃ on rutile is observed. As α -Al₂O₃ and TiO₂ rutile structures can be both considered as being composed of close-packed oxygen layers with cations distributed in octahedral sites, the atomic arrangement are surmised to play a critical role in controlling the properties of the stack α -Al₂O₃/rutile during the initial growth stages of α -Al₂O₃ [38]. Fig. 7 (c) and (d) illustrate the epitaxial relationships at the rutile/ α -Al₂O₃ interface. Similar relationships have also been reported previously, where rutile thin films are epitaxially grown on α -Al₂O₃ substrates by reactive ionized cluster beam deposition

(RICBD) or metalorganic chemical vapor deposition (MOCVD) [38–40]. Although different deposition techniques are used, the epitaxial growth at the α -Al₂O₃/rutile interface is always highlighted.

Firstly, the lattice mismatch for $(10\bar{1})_{\text{rutile}}$ and $(\bar{1}20)_{\alpha\text{-Al}_2\text{O}_3}$ with the in-plane orientations $[101]_{\text{rutile}}$ and $[210]_{\alpha\text{-Al}_2\text{O}_3}$ is low, less than a few percent [38]. Meanwhile, according to the structural mismatch schema at the rutile/ α -Al₂O₃ interface proposed by Danu *et al.*, an ideal fitting region is shown, while an A- (or B-) type oxygen layer of α -Al₂O₃ faces an A- (or B-) type oxygen layer of rutile [41]. Secondly, it is found that rutile film consists of three equal domains rotated by 120° [37]. The reason behind this particular arrangement is that a tetragonal unit cell with a 2-fold symmetry matches with a hexagonal unit cell with a 3-fold symmetry in the stack rutile/ α -Al₂O₃. It is shown that $[101]_{\text{rutile}}$ can orient with any of the three equivalent $[210]_{\alpha\text{-Al}_2\text{O}_3}$ directions of $(001)_{\alpha\text{-Al}_2\text{O}_3}$ [40]. Thus, the orientation relationships experimentally found can now be explained.

Fig. 8 (a) shows a cross-section STEM HAADF micrograph of sample **C**, Fig. 8 (b) presents EELS mapping acquired from the black square indicated in Fig. 8 (a). As shown in Fig. 8 (a), no evidence for oxide phases can be found at the bonding/Al₂O₃ layers interface, while Ti(C,N) needle-shaped grains are observed. It is reported that CO addition results in the incorporation of oxygen into the Ti(C,N) phase leading to the microstructure refinement, but the C/N ratio and the lattice parameter of the Ti(C,N) phase will not be affected [1]. However, EELS analysis shows that no evidence for oxide

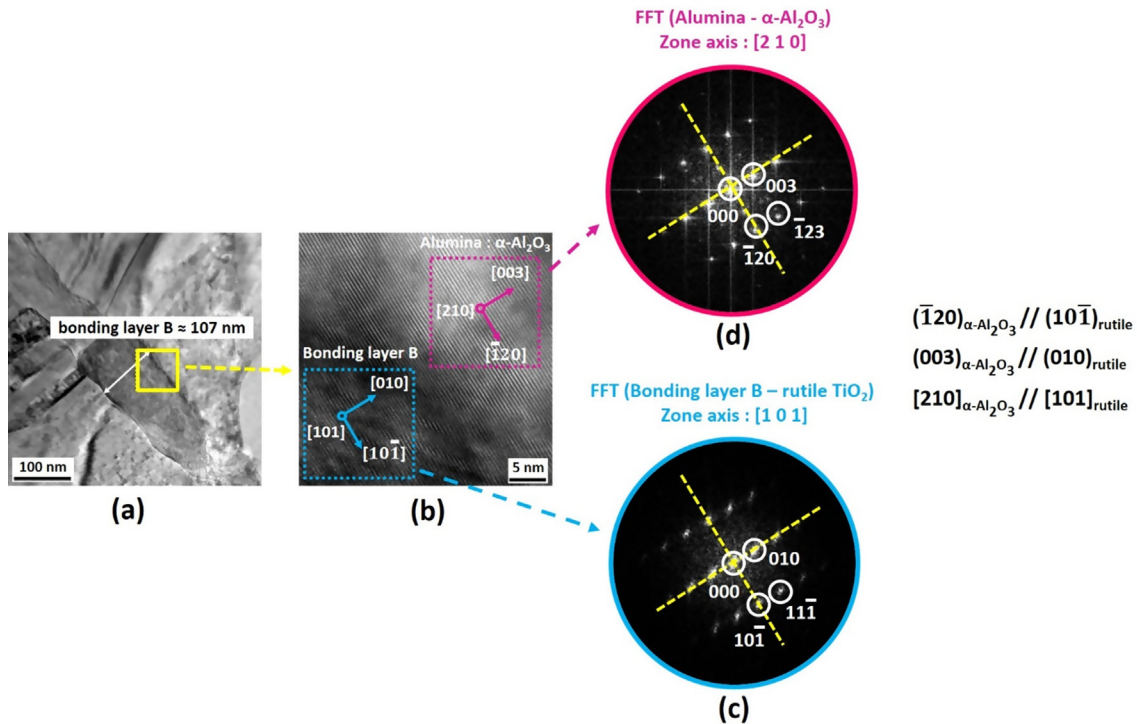


Fig. 7. (a) TEM BF image showing the bonding/ α -Al₂O₃ layers interface of sample **B**. (b) HRTEM image acquired from the yellow square indicated in (a). (c) and (d) Fast Fourier Transform (FFT) images obtained from the blue (bonding layer) and red (α -Al₂O₃ layer) dashed squares indicated in (b), the orientation relationships are illustrated by yellow dashed lines. (For interpretation of the references to colour in this figure legend, the reader is referred to the web version of this article.)

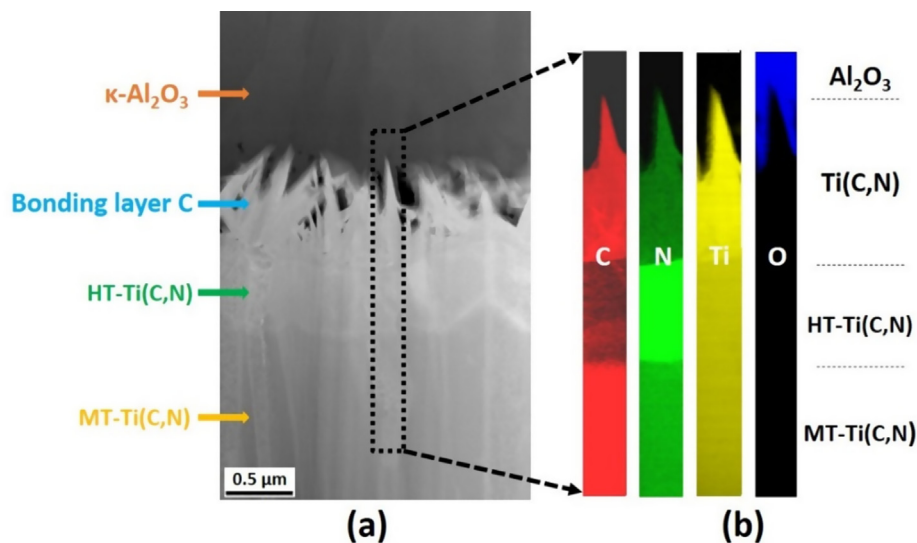


Fig. 8. (a) STEM HAADF image showing a cross-section of sample **C**. (b) EELS mapping acquired from the black square indicated in (a).

phases can be detected in the bonding layer. Hence, it is believed that the microstructure of bonding layer **C** is more likely dependent on the deposition temperature and the CH₄/N₂ ratio of the gas mixture used, according to Cheng et al [36].

Fig. 9 (a) shows a cross-section TEM BF image of sample **C**, and Fig. 9 (b) is a TEM BF image with lower magnification to present the Al₂O₃ layer near the coating surface. Fig. 9 (b.1) is a SAED pattern acquired from the orange circle area indicated in Fig. 9 (b). It is shown that pure κ -Al₂O₃ is obtained. Fig. 9 (c) shows a TEM BF image acquired from the red area indicated in Fig. 9 (a). Fig. 9 (c.1) and (c.2) are micro-diffraction and SAED patterns acquired

from the blue (bonding layer **C**) and orange (κ -Al₂O₃ layer) circle areas at the interface indicated in Fig. 9 (c), which confirm the nucleation of κ -Al₂O₃ on Ti(C,N) (bonding layer **C**). Since Ti(C,N) needle-shaped grains are extremely fine, the superposition of spots could falsify the result, the micro-diffraction was used.

Fig. 10 (a) shows the TEM image at the bonding/ κ -Al₂O₃ layers interface, Ti(C,N) needle-shaped grains are observed. Fig. 10 (b) is the HRTEM image obtained from the yellow dashed square indicated in Fig. 10 (a). Fast Fourier Transform (FFT) images acquired from the green, blue and red dashed squares indicated in Fig. 10 (b) are shown in Fig. 10 (c)-(e), it is shown that Ti(C,N) needle-

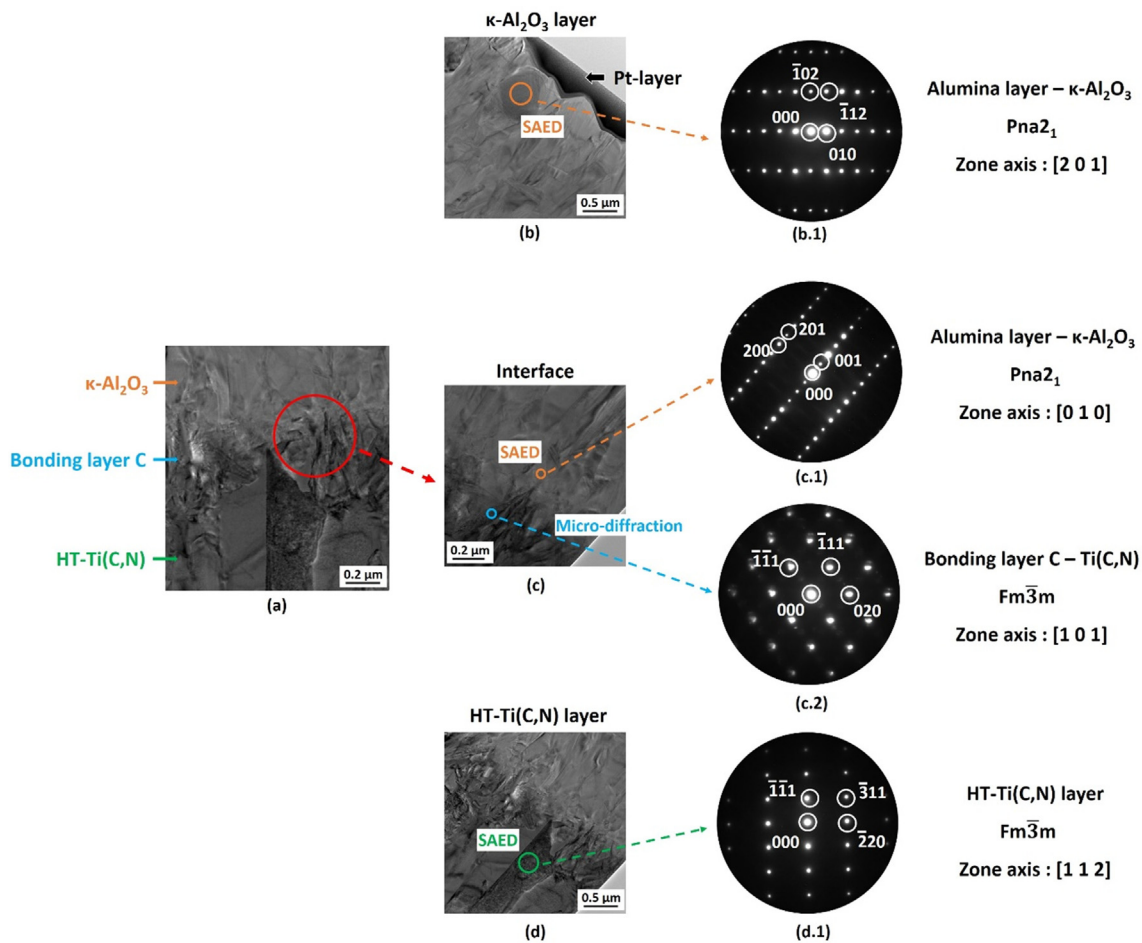


Fig. 9. (a) TEM BF image showing a cross-section overview of sample C, needle-shaped grains developed at the bonding/ $\kappa\text{-Al}_2\text{O}_3$ layers interface. (b) and (d) TEM BF images showing the $\kappa\text{-Al}_2\text{O}_3$ and HT-Ti(C,N) layers. (c) TEM BF image obtained from the red circle area at the bonding/ $\kappa\text{-Al}_2\text{O}_3$ layers interface indicated in (a). (b.1)-(d.1) SAED patterns corresponding to differently grown layers. (c.2) Micro-diffraction image of the bonding layer. (For interpretation of the references to colour in this figure legend, the reader is referred to the web version of this article.)

shaped grains consist of twin-related domains with the growth of parallel {111} planes.

Fig. 11 (a) shows the TEM BF image at the bonding/ $\kappa\text{-Al}_2\text{O}_3$ layers interface. Fig. 11 (b) presents the HRTEM image acquired from the red square indicated in Fig. 11 (a). Fig. 11 (c) and (d) are FFT images acquired from the blue and orange squares indicated in Fig. 11 (b). As has been discussed by Liu *et al.*, the oxygen sublattice in $\kappa\text{-Al}_2\text{O}_3$ with an -ABAC- stacking sequence has the space group P6₃/mmc, and the positions of Al-ions reduce the symmetry to Pna2₁ [16]. Several studies show that alumina deposition on TiN {111} planes yields generally the epitaxial growth of {001} $\kappa\text{-Al}_2\text{O}_3$ close-packed planes, with directions parallel in these two phases, e.g. [010] _{$\kappa\text{-Al}_2\text{O}_3$} //[110]_{TiN}, the misfit is about 9% [26,27]. According to Halvarsson *et al.*, if oxygen ions occupy A-positions, titanium ions can be placed in interstitial B- or C-positions on the close-packed oxygen plane, TiN crystals can be formed with an -ABCABC- or -ACBACB- stacking sequence [26]. It is similar to that found in Fig. 9 (c.1) and (c.2), the orientation relationships can be expressed as: (001) _{$\kappa\text{-Al}_2\text{O}_3$} //($\bar{1}$ 11)_{Ti(C,N)} and [010] _{$\kappa\text{-Al}_2\text{O}_3$} //[101]_{Ti(C,N)}. The atomic arrangement schema of (001) $\kappa\text{-Al}_2\text{O}_3$ created by software VESTA is given in Supplementary Fig. S2.

Furthermore, the epitaxial growth at the lateral interface of bonding layer C is also observed, with different orientation relationships found as: (100) _{$\kappa\text{-Al}_2\text{O}_3$} //($\bar{1}$ 11)_{Ti(C,N)}, (013) _{$\kappa\text{-Al}_2\text{O}_3$} //(220)_{Ti(C,N)} and [031] _{$\kappa\text{-Al}_2\text{O}_3$} //[112]_{Ti(C,N)}. It is reported earlier that the surface morphology of bonding layer may be responsible for the phase composition of Al_2O_3 [15,42]. It shows that when the bonding layer consists of needle shaped grains, with needles almost parallel to the deposition direction, the nucleation of $\alpha\text{-Al}_2\text{O}_3$ is favored. Conversely, the formation of a nano-transition needle-like phase is also proved to promote the growth of $\kappa\text{-Al}_2\text{O}_3$ [4]. Thereby, it is believed that the effect of surface morphology of bonding layers can be discarded. To verify the orientation relationships, the arrangement of O-atoms in the plane (100) _{$\kappa\text{-Al}_2\text{O}_3$} along the direction [031] and Ti-atoms in the plane ($\bar{1}$ 11)_{Ti(C,N)} along the direction [112] are illustrated by VESTA (see Fig. 12), and the Crystallography Open Database files 1,000,442 and 1,540,253 corresponding to $\kappa\text{-Al}_2\text{O}_3$ and Ti(C,N) phases are used. It is speculated that the crystallographic arrangement may control the properties of the stack $\kappa\text{-Al}_2\text{O}_3$ /Ti(C,N) during the initial growth stage of $\kappa\text{-Al}_2\text{O}_3$. The distance between every two O-atoms and Ti-atoms at the interface is calculated and pre-

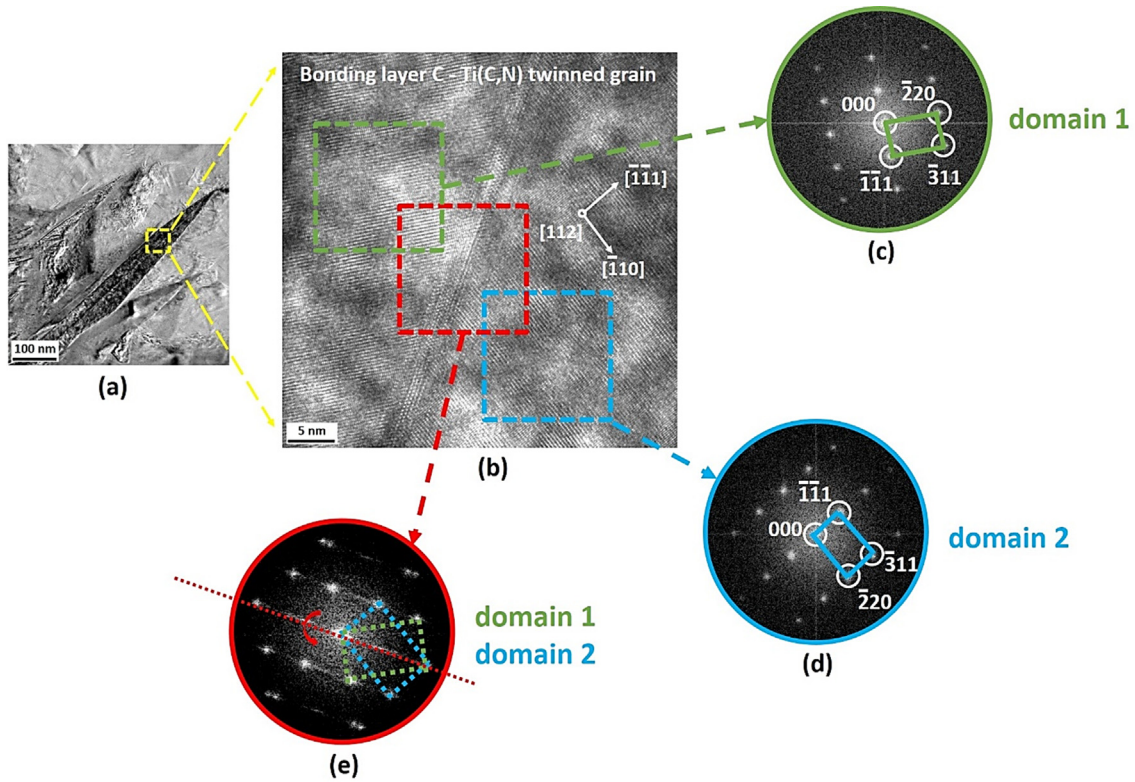


Fig. 10. (a) TEM BF image showing the bonding layer of sample C composed of fine needle-shaped grains. (b) HRTEM image obtained from the yellow area indicated in (a), and the twin boundary can be seen from the bottom left corner to the top right corner. (c)-(e) Fast Fourier Transform (FFT) images along [1 1 2] projection, obtained from dashed squares indicated in (b). (For interpretation of the references to colour in this figure legend, the reader is referred to the web version of this article.)

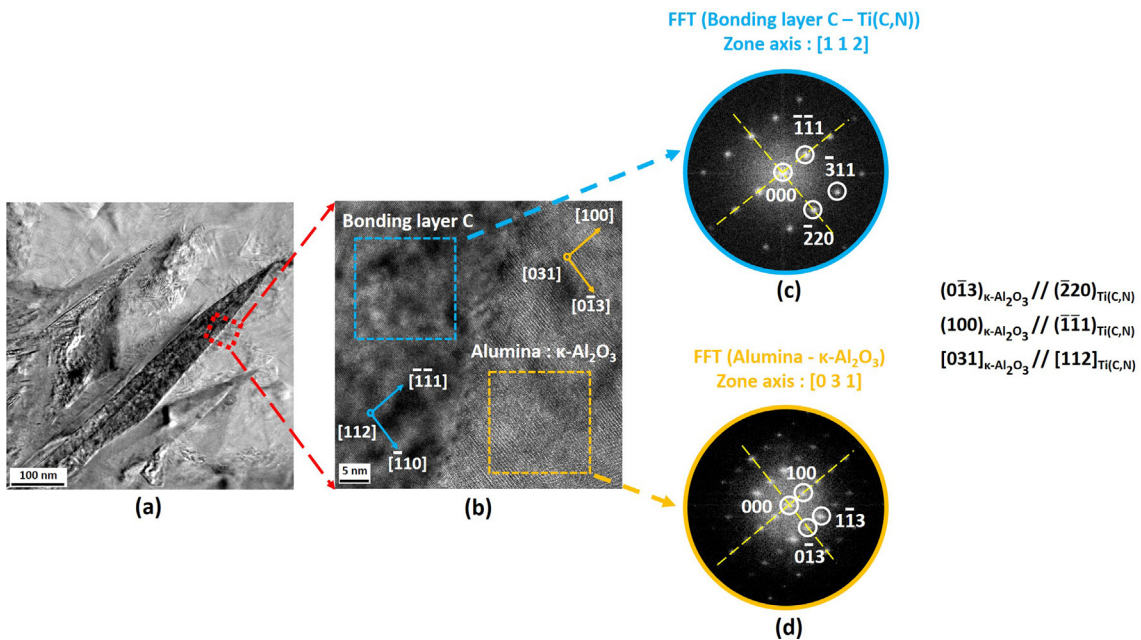


Fig. 11. (a) TEM BF image showing the bonding layer of sample C. (b) HRTEM image obtained from the red square area indicated in (a). (c) and (d) Fast Fourier Transform (FFT) images acquired from the blue (bonding layer C) and orange ($\kappa\text{-Al}_2\text{O}_3$) layer square areas indicated in (b), the orientation relationships are illustrated by yellow dashed lines. (For interpretation of the references to colour in this figure legend, the reader is referred to the web version of this article.)

sented in Fig. 12, the mismatch is about 7%, and slightly lower mismatch is obtained for $(0\bar{1}3)_{\kappa\text{-Al}_2\text{O}_3}$ and $(\bar{2}20)_{\text{Ti(C,N)}}$. Hence, the basic mechanism explaining why the nucleation of $\kappa\text{-Al}_2\text{O}_3$ is favored in sample C can be clearly explained.

4. Conclusions

In this work, a series of CVD Al_2O_3 coatings were deposited without (sample A) and with different bonding layers (samples B

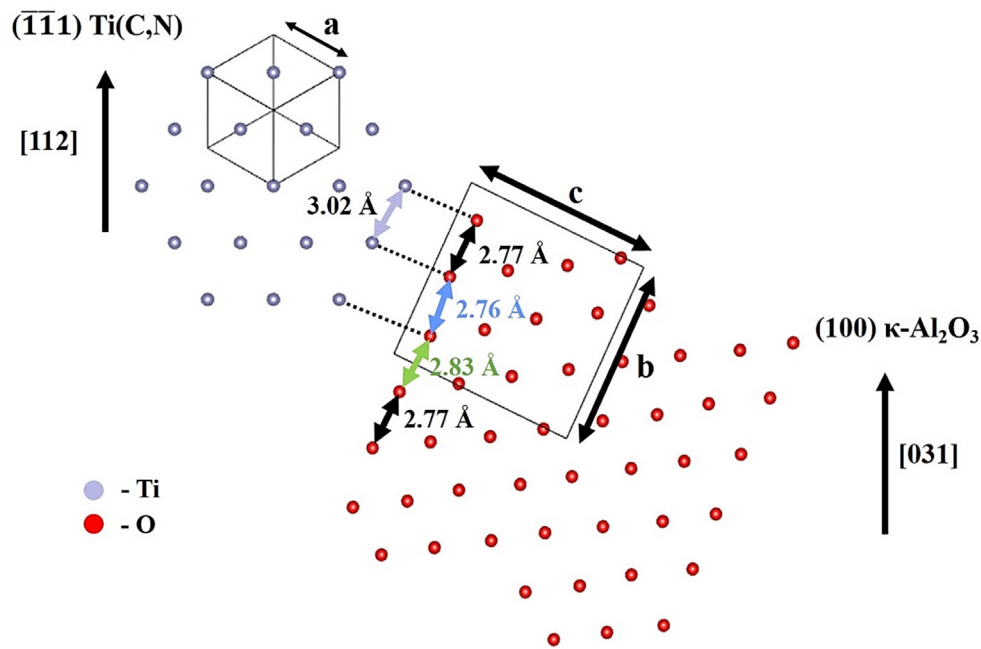


Fig. 12. Schematic crystallographic arrangement of O-atoms in the plane $(100)_{\kappa-Al_2O_3}$ along the direction $[031]$, and Ti-atoms in the plane $(\bar{1}\bar{1}1)_{Ti(C,N)}$ along the direction $[112]$.

and C). Two other samples **B1** and **C1** were stopped after synthesis of the bonding layers **B** and **C**. The interfacial microstructures were investigated in detail, and main results can be summarized as follows:

- (1) The Al_2O_3 layer in sample **A** was deposited on the non-oxidized HT-Ti(C,N) layer, pure $\alpha-Al_2O_3$ is obtained, but no orientation relationships at the interface can be observed. Thus, it can be concluded that $\alpha-Al_2O_3$ is the preferred alumina phase to be deposited with the deposition conditions used in this work, as it is the most thermodynamically stable phase.
- (2) The Al_2O_3 layer in sample **B** was deposited on the bonding layer **B** consisting of rutile, $\alpha-Al_2O_3$ is epitaxially grown on rutile, and the orientation relationships can be expressed as: $(\bar{1}20)_{\alpha-Al_2O_3} // (10\bar{1})_{rutile}$, $(003)_{\alpha-Al_2O_3} // (010)_{rutile}$ and $[210]_{\alpha-Al_2O_3} // [101]_{rutile}$.
- (3) Regarding sample **C**, pure $\kappa-Al_2O_3$ is obtained, due to the epitaxial growth of $\kappa-Al_2O_3$ on Ti(C,N) with the epitaxial relationships found as: $(100)_{\kappa-Al_2O_3} // (\bar{1}\bar{1}1)_{Ti(C,N)}$, $(0\bar{1}3)_{\kappa-Al_2O_3} // (\bar{2}20)_{Ti(C,N)}$ and $[031]_{\kappa-Al_2O_3} // [112]_{Ti(C,N)}$. It is believed that it is necessary to satisfy the epitaxial growth of $\kappa-Al_2O_3$ on Ti(C,N) to promote the nucleation of $\kappa-Al_2O_3$, otherwise, $\alpha-Al_2O_3$ is the preferred alumina phase to be deposited with the deposition conditions used.
- (4) Since processing parameters for the alumina deposition were always the same, and the epitaxial growth of $\alpha-Al_2O_3$ on rutile as well as that of $\kappa-Al_2O_3$ on Ti(C,N) are evidenced, it is revealed that the nucleation of $\alpha-Al_2O_3$ and $\kappa-Al_2O_3$ can be accurately controlled with different treatments of the nucleation surface.

Declaration of Competing Interest

The authors declare that they have no known competing financial interests or personal relationships that could have appeared to influence the work reported in this paper.

Acknowledgements

The authors would like to acknowledge assistance from the Institut Jean Lamour and the Groupement d'Intérêt Public Haute-Marne (GIP 52) for their support. Special thanks to Sylvie Migot (CC3M -Institut Jean Lamour) for FIB/SEM investigations and Jaafar Ghanbaja (CC3M-Institut Jean Lamour) for the insightful discussions.

Appendix A. Supplementary material

Supplementary data to this article can be found online at <https://doi.org/10.1016/j.matdes.2022.110601>.

References

- [1] C. Czettl, C. Mitterer, U. Mühle, D. Rafaja, S. Puchner, H. Hutter, M. Penoy, C. Michotte, M. Kathrein, CO addition in low-pressure chemical vapor deposition of medium-temperature TiC_xN_{1-x} based hard coatings, *Surf. Coat. Technol.* 206 (2011) 1691–1697, <https://doi.org/10.1016/j.surfcoat.2011.07.086>.
- [2] S. Rупpi, Deposition, microstructure and properties of texture-controlled CVD $\alpha-Al_2O_3$ coatings, *Int. J. Refract. Met. H.* 23 (2005) 306–316, <https://doi.org/10.1016/j.ijrmhm.2005.05.004>.
- [3] R. Stylianou, M. Tkadletz, N. Schalk, M. Penoy, C. Czettl, C. Mitterer, Effects of reference materials on texture coefficients determined for a CVD $\alpha-Al_2O_3$ coating, *Surf. Coat. Technol.* 359 (2019) 314–322, <https://doi.org/10.1016/j.surfcoat.2018.12.095>.
- [4] C. Barbatti, J. Garcia, R. Pitonak, H. Pinto, A. Kostka, A. Di Prinzio, M.H. Staia, A. R. Pyzalla, Influence of micro blasting on the microstructure and residual stresses of CVD $\kappa-Al_2O_3$ coatings, *Surf. Coat. Technol.* 203 (2009) 3708–3717, <https://doi.org/10.1016/j.surfcoat.2009.06.021>.
- [5] Z.-J. Liu, Z.-K. Liu, C. McNerny, P. Mehrotra, A. Inspektor, Investigations of the bonding layer in commercial CVD coated cemented carbide inserts, *Surf. Coat. Technol.* 198 (1–3) (2005) 161–164, <https://doi.org/10.1016/j.surfcoat.2004.10.112>.
- [6] M. Fallqvist, S. Rупpi, M. Olsson, M. Ottosson, T.M. Grehk, Nucleation and growth of CVD $\alpha-Al_2O_3$ on Ti_xO_y template, *Surf. Coat. Technol.* 207 (2012) 254–261, <https://doi.org/10.1016/j.surfcoat.2012.06.087>.
- [7] I.E. Azhari, J. Garcia, M. Zamanzade, F. Soldera, C. Pauly, C. Motz, L. Lianes, F. Mücklich, Micromechanical investigations of CVD coated WC-Co cemented carbide by micropillar compression, *Mater. Des.* 186 (2020) 108283, <https://doi.org/10.1016/j.matdes.2019.108283>.
- [8] D. Hochauer, C. Mitterer, M. Penoy, S. Puchner, C. Michotte, H.P. Martnz, H. Hutter, M. Kathrein, Carbon doped $\alpha-Al_2O_3$ coatings grown by chemical vapour

- deposition, *Surf. Coat. Technol.* 206 (2012) 4771–4777, <https://doi.org/10.1016/j.surfcoat.2012.03.059>.
- [9] M. Halvarsson, A. Larsson, S. Rupp, Study of the interfacial structure and chemistry of CVD κ -Al₂O₃/TiC multilayer coatings, *Micron*. 32 (2001) 807–815, [https://doi.org/10.1016/S0968-4328\(00\)00088-3](https://doi.org/10.1016/S0968-4328(00)00088-3).
- [10] T. Shen, L. Zhu, Z. Liu, Effect of micro-blasting on the tribological properties of TiN/MT-Ti(C, N)/Al₂O₃/TiCNO coatings deposited by CVD, *Int. J. Refract. Met H.* 88 (2020) 105205, <https://doi.org/10.1016/j.ijrmhm.2020.105205>.
- [11] M.T. Swihart, L. Catoire, Reactions in the Al-H-Cl system studied by ab initio molecular orbital and density functional methods, *J. Phys. Chem. A*. 105 (2001) 264–273, <https://doi.org/10.1021/jp003526e>.
- [12] F. Konstantiniuk, M. Tkadletz, C. Kainz, C. Czettl, N. Schalk, Mechanical properties of single and polycrystalline α -Al₂O₃ coatings grown by chemical vapour deposition, *Surf. Coat. Technol.* 410 (2021) 126959, <https://doi.org/10.1016/j.surfcoat.2021.126959>.
- [13] S. Rupp, Influence of process conditions on the growth and texture of CVD alpha-alumina, *Coatings*. 10 (2020) 158, <https://doi.org/10.3390/coatings10020158>.
- [14] A. Blomqvist, C. Arhammar, H. Pedersen, F. Silvearv, S. Norgren, R. Ahuja, Understanding the catalytic effects of H₂S on CVD-growth of α -alumina: Thermodynamic gas-phase simulations and density functional theory, *Surf. Coat. Technol.* 206 (7) (2011) 1771–1779, <https://doi.org/10.1016/j.surfcoat.2011.09.018>.
- [15] S. Shoja, N. Mortazavi, E. Lindahl, S. Norgren, O. Bäcke, M. Halvarsson, Microstructure investigation of textured CVD alumina coatings, *Int. J. Refract. Met H.* 87 (2020) 105125, <https://doi.org/10.1016/j.ijrmhm.2019.105125>.
- [16] P. Liu, J. Skogsmo, Space-group determination and structure model for κ -Al₂O₃ by convergent-beam electron diffraction, *Acta Cryst B*. 47 (1991) 425–433, <https://doi.org/10.1107/S010876819100071X>.
- [17] M.L. Kronberg, Plastic deformation of single crystals of sapphire: basal slip and twinning, *Acta Metall.* 5 (1957) 507–524, <https://doi.org/10.1007/978-1-4899-1441-5>.
- [18] S. Vuorinen, L. Karlsson, Phase transformation in chemically vapour-deposited κ -alumina, *Thin Solid Films* 214 (2) (1992) 132–143, [https://doi.org/10.1016/0040-6090\(92\)90761-Y](https://doi.org/10.1016/0040-6090(92)90761-Y).
- [19] S. Rupp, A. Larsson, A. Flink, Nanoindentation hardness, texture and microstructure of α -Al₂O₃ and κ -Al₂O₃ coatings, *Thin Solid Films*. 516 (2008) 5959–5966, <https://doi.org/10.1016/j.tsf.2007.10.078>.
- [20] P. Martensson, Influence of the concentration of ZrCl₄ on texture, morphology and growth rate of CVD grown α -Al₂O₃ coatings deposited by the AlCl₃/ZrCl₄/H₂/CO₂/H₂S process, *Surf. Coat. Technol.* 200 (2006) 3626–3632, <https://doi.org/10.1016/j.surfcoat.2005.01.008>.
- [21] S. Canovic, S. Rupp, J. Rohrer, A. Vojvodic, C. Ruberto, P. Hyldegaard, M. Halvarsson, TM and DFT investigation of CVD TiN/ κ -Al₂O₃ multilayer coatings, *Surf. Coat. Technol.* 202 (2007) 522–531, <https://doi.org/10.1016/j.surfcoat.2007.06.022>.
- [22] S. Canovic, B. Ljungberg, C. Björmander, M. Halvarsson, CVD TiC/alumina and TiN/alumina multilayer coatings grown on sapphire single crystals, *Int. J. Refract. Met H.* 28 (2) (2010) 163–173, <https://doi.org/10.1016/j.ijrmhm.2009.08.001>.
- [23] S. Canovic, B. Ljungberg, M. Halvarsson, CVD TiC/alumina multilayer coatings grown on sapphire single crystals, *Micron*. 42 (2011) 808–818, <https://doi.org/10.1016/j.micron.2011.05.003>.
- [24] R.M. Saoubi, O. Alm, J.M. Andersson, H. Engström, T. Larsson, M.P. Johansson-Jöesaar, M. Schwind, Microstructure and wear mechanisms of texture-controlled CVD α -Al₂O₃ coatings, *Wear* 376 (377) (2017) 1766–1778, <https://doi.org/10.1016/j.wear.2017.01.071>.
- [25] R. Stylianou, D. Velic, W. Daves, W. Ecker, M. Tkadletz, N. Schalk, C. Czettl, C. Mitterer, Thermal crack formation in TiCN/ α -Al₂O₃ bilayer coatings grown by thermal CVD on WC-Co substrates with varied Co content, *Surf. Coat. Technol.* 392 (2020), <https://doi.org/10.1016/j.surfcoat.2020.125687>.
- [26] M. Halvarsson, S. Vuorinen, Microstructural investigations of CVD TiN/ κ -Al₂O₃ multilayer coatings on cemented carbides, *Int. J. Refract. Met H.* 15 (1997) 169–178, [https://doi.org/10.1016/S0263-4368\(96\)00028-5](https://doi.org/10.1016/S0263-4368(96)00028-5).
- [27] M. Halvarsson, J.E. Trancik, S. Rupp, The microstructure of CVD κ -Al₂O₃ multilayers separated by thin intermediate TiN or TiC layers, *Int. J. Refract. Met H.* 24 (1–2) (2006) 32–38, <https://doi.org/10.1016/j.ijrmhm.2005.06.007>.
- [28] F. Uny, S. Achache, S. Lamri, J. Ghanbaja, E. Fischer, M. Pons, E. Blanquet, F. Schuster, F. Sanchette, Deposition and characterization of (Ti, Al)N coatings deposited by thermal LPCVD in an industrial reactor, *Surf. Coat. Technol.* 358 (2019) 923–933, <https://doi.org/10.1016/j.surfcoat.2018.12.014>.
- [29] M. Zhu, S. Achache, P. Boulet, A. Virfeu, J.-F. Pierson, F. Sanchette, Effects of deposition parameters on the microstructure and mechanical properties of Ti (C, N) produced by moderate temperature chemical vapor deposition (MT-CVD) on cemented carbides, *Vacuum* 195 (2022) 110650, <https://doi.org/10.1016/j.vacuum.2021.110650>.
- [30] C. Kainz, N. Schalk, M. Tkadletz, M. Winkler, C. Czettl, Microstructure, mechanical and thermos-physical properties of TiC_xN_{1-x} coatings on cemented carbide substrates grown with C₂H₆ as C feeding precursor, *Surf. Coat. Technol.* 394 (2020) 125868, <https://doi.org/10.1016/j.surfcoat.2020.125868>.
- [31] E. Breval, S. Vuorinen, Structure and hardness of titanium carbide coatings on hard metals, *Mater. Sci. Eng.* 42 (1980) 361–366, [https://doi.org/10.1016/0025-5416\(80\)90046-4](https://doi.org/10.1016/0025-5416(80)90046-4).
- [32] D.H. Trinh, K. Back, G. Pozina, H. Blomqvist, T. Selinder, M. Collin, I. Reineck, L. Hultman, H. Högberg, Phase transformation in κ - and γ -Al₂O₃ coatings on cutting tool inserts, *Surf. Coat. Technol.* 203 (12) (2009) 1682–1688, <https://doi.org/10.1016/j.surfcoat.2008.12.028>.
- [33] D. Hochauer, C. Mitterer, M. Penoy, C. Michotte, H.P. Martinz, M. Kathrein, Thermal stability of doped CVD κ -Al₂O₃ coatings, *Surf. Coat. Technol.* 204 (2010) 3713–3722, <https://doi.org/10.1016/j.surfcoat.2010.04.056>.
- [34] I.E. Azhari, J. Garcia, M. Zamanzade, F. Soldera, C. Pauly, C. Motz, L. Lianes, F. Mücklich, Investigations on micro-mechanical properties of polycrystalline Ti (C, N) and Zr(C, N) coatings, *Acta Mater.* 149 (2018) 364–376, <https://doi.org/10.1016/j.actamat.2018.02.053>.
- [35] L.C. Qiu, Y. Du, S.Q. Wang, L.Y. Du, Z. Chen, J. Wang, Z.Q. Zhong, H.D. Shi, L. Albir, Through-process modelling and experimental verification of titanium carbonitride coating prepared by moderate temperature chemical vapour deposition, *Surf. Coat. Technol.* 359 (2019) 278–288, <https://doi.org/10.1016/j.surfcoat.2018.12.096>.
- [36] D.-J. Cheng, W.-P. Sun, M.-H. Hon, The morphology and structure of chemically vapour-deposited Ti(C, N) coatings, *Thin Solid Films* 146 (1) (1987) 45–53, [https://doi.org/10.1016/0040-6090\(87\)90338-5](https://doi.org/10.1016/0040-6090(87)90338-5).
- [37] M.R. Bayati, R. Molaei, R.J. Narayan, J. Narayan, H. Zhou, S.J. Pennycook, Domain epitaxy in TiO₂/ α -Al₂O₃ thin film heterostructures with Ti₂O₃ transit layer, *Appl. Phys. Lett.* 100 (2012) 251606, <https://doi.org/10.1063/1.4729937>.
- [38] P.A.M. Hotsenpiller, A. Roshko, J.B. Lowekamp, G.S. Rohrer, Growth morphologies of heteroepitaxial rutile films on sapphire substrates, *J. Cryst Growth*. 174 (1–4) (1997) 424–433, [https://doi.org/10.1016/S0022-0248\(96\)01138-4](https://doi.org/10.1016/S0022-0248(96)01138-4).
- [39] D.R. Burgess, P.A. Morris Hotsenpiller, T.J. Anderson, J.L. Hohman, Solid precursor MOCVD of heteroepitaxial rutile phase TiO₂, *J. Cryst Growth*. 166 (1996) 763–768, [https://doi.org/10.1016/0022-0248\(95\)00538-2](https://doi.org/10.1016/0022-0248(95)00538-2).
- [40] M.R. Bayati, S. Joshi, R.J. Narayan, J. Narayan, Low-temperature processing and control of structure and properties sapphire epitaxial heterostructures, *J. Mater. Res.* 28 (2013) 1669–1679, <https://doi.org/10.1557/jmr.2013.42>.
- [41] N. Daneu, A. Recnik, W. Mader, Atomic structure and formation mechanism of (101) rutile twins from Diamantina, *Am. Mineral.* 99 (2014) 612–624, <https://doi.org/10.2138/am.2014.4672>.
- [42] M. Halvarsson, H. Nordén, S. Vuorinen, Microstructural investigation of CVD α -Al₂O₃/ κ -Al₂O₃ multilayers coatings, *Surf. Coat. Technol.* 61 (1993) 177–181, [https://doi.org/10.1016/0257-8972\(93\)90222-8](https://doi.org/10.1016/0257-8972(93)90222-8).